

A Data-Driven Model for the Field Emission from Broad-Area Electrodes

Moein Borghei, Robin Langtry

^a*Avalanche Energy, 9100 E Marginal Way S, Tukwila, 98108, WA, USA*

Abstract

Electron emission from cathodes in high field gradients is a quantum tunneling effect. The Fowler-Nordheim (FN) equation has traditionally been key in describing cold-field emissions, offering estimates for emitters for almost a century. Nevertheless, applying FN theory in practice is often constrained by the lack of data on the distribution and geometry of the emission sites. Predictions become more challenging with an uneven electric field distribution at the cathode surface. Consequently, FN formulations are frequently calibrated using current-voltage data after test, reducing their effectiveness as truly predictive models.

This study proposes the development of a data-informed predictive model of field emission that leverages (1) vast experimental data, (2) electrostatic simulations of the cathode surface, and (3) detailed material and geometric properties to overcome these limitations. The goal is to harness this comprehensive dataset to train a machine learning model capable of providing precise predictions of the cathode current, thereby enhancing the understanding and application of field emission phenomena. More than 259 hours of experimental data have been processed to train and benchmark some of the well-known machine learning models. After two stages of optimization, a coefficient of determination $> 98\%$ is achieved in the prediction total field emission current using ensemble models.

Keywords: field emission, Fowler-Nordheim theory, machine learning, quantum tunneling

1. Introduction

Conductors are often used to transport electrical charges. In most applications, these electrons are totally confined within the material by the presence of a surface potential barrier known as the material's work function. Until the early twentieth century, the emission of electrons from conductors was engineered through thermionic and photoelectric emission processes.

In the 1920s, first, J.E. Lillienfeld [1] and then, W. D. Coolidge [2] recognized another phenomenon of electron emission from the cold cathode due to the high electric field strength at the surface. Following a series of experimental and theoretical works [3, 4, 5, 6, 7], Fowler and Nordheim derived a closed-form equation for the current density of an emission site [8]. Based on the 1D Schrödinger equation, Fowler-Nordheim derived a numerical approximation to determine the tunneling rate of elec-

trons through the potential barrier as a function of the local electric field and material work function.

In the Fowler-Nordheim equation, the field enhancement factor and the emitting surface area are two crucial parameters. Traditionally, field emission is explained by field enhancement on a sharp metallic whisker, which can be created artificially or developed through surface dislocation activity [9] or surface diffusion [10] under high field strength. Several efforts have been made to approximate the shape of field enhancing features [11, 12, 13, 14]. Nevertheless, the detection of field emission current on an extremely polished cathode surface indicates alternative sources of field emission apart from whiskers, as validated by the observations in [15], along with the shift in electron emission spectra to energies below the Fermi level [16, 17] and the cathode electroluminescence [18], all pointing towards a non-metallic origin.

Aside from the debates over the origin of the field emission current, nearly a century later after the discovery of the field emission, there is still no widely accepted model for the prediction of total

Email address: mborghei@avalanchefusion.com
(Moein Borghei)

field emission for practical applications involving broad-area electrodes, large gaps, and nonuniform electric field distribution where numerous emission sites make up the total field emission current, also known as *dark current*. In practice, it is nearly impossible to acquire all the geometric details about microscopic emission sites on a broad-area electrode.

In this work, our aim is to train a data-driven model based on more than 259 hours of experimental data. We supplement the input dataset with electrostatic, geometrical, and material information about the cathode. The model is agnostic about the individual field emission sites and aims at recognizing their collective pattern on a broad-area electrode. To complement the cathode voltage and current measurements, we utilize the electric field distribution from an electrostatic simulation, which yields statistical features that explain the probability distribution of the electric field magnitude. Optical microscopy of a $1\ \mu\text{m} \times 1\ \mu\text{m}$ section of a cathode data provides statistical features of the projection heights of the surface structure. Lastly, the work function of the material and the total cathode area conclude the input dataset.

Relaxing the modeling of broad-area emission from the traditional curve fitting to a more data-informed complex model allows one to capture a wider variation of data. Moreover, such a model can be constantly reinforced with more test results, provided that the aforementioned set of data is provided. Performance comparison of different supervised machine learning on the dataset shows that we can achieve $> 98\%$ accuracy in the prediction of the total field emission current with the gradient boosting ensemble model.

The structure of the remainder of this article is delineated as follows: In Section 2, we provide a comprehensive review of the Fowler-Nordheim theory and its extension to accommodate a multiplicity of emitters. Section 3 elucidates the framework of our approach to field emission prediction, which will be discussed in more detail in subsequent sections. The experimental setup is briefly discussed in Section 4. Section 5 details the preprocessing of data for application in machine learning models. The results of training and testing various machine learning models with the constructed dataset are presented in Section 6. Finally, a discussion of the results and the conclusions are presented in Sections 7 and 8, respectively.

2. Overview of Fowler-Nordheim Theory

Fowler and Nordheim [8] used quantum tunneling theory to calculate the probability that an electron escapes from a metal surface under a high electric field, which is then integrated into the energy states to obtain the emission current density. The following is the approximate current density equation:

$$J = \frac{C_1 E^2}{\phi t(y)^2} e^{-\frac{C_2 \phi^{3/2} v(y)}{E}} \quad (1)$$

where C_1 and C_2 are constants; E is the intensity of the local electric field at the emitter and ϕ is the material work function. Finally, $t(y)$ and $v(y)$ are slowly varying functions of ϕ and E that are typically very close to unity [19].

If one knows the emitting area of an emission site, A , the total current from the emission site, I , can be computed by multiplying the current density and the emitting area.

2.1. Characteristics of a single emission site

The electric field at the emission site, denoted E , frequently exceeds the anticipated magnitude derived from the estimation of the macroscopic field E_0 , by two to three orders of magnitude. Consequently, an enhancement factor, β , is typically used to approximate the microscopic electric field, such that $E = \beta E_0$. The effective field enhancement factor of a single emission site can be defined as [20]:

$$\beta = \frac{1}{I} \int_S \beta(\mathbf{x}) J(\mathbf{x}) dS \quad (2)$$

In practical cases, only after acquiring the $I - V$ measurement can the field enhancement factor be derived from the linear slope of $\log(I/E^2)$ versus $1/E$. For many, this has been the confirmation of the famous whisker model that originated in the mid-60s that the applied macroscopic field is geometrically enhanced by a factor at the tip of a whisker to reach the required threshold and the microscopic electric field exceeds the threshold value of $3\ \text{GV}/\text{m}$. As mentioned in Section 1, some experimental results have shown that the emission came from a more complex regime involving an insulating microinclusion as shown in Figure 1.

2.2. From Single Emitter to Multiple Emitters

In practical applications, the measured field emission current includes the contribution of not one

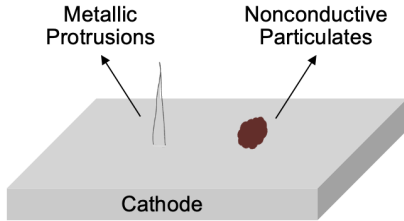


Figure 1: Exemplary illustration of the field enhancement features.

but many emitters. Ideally, the field enhancement factor, work function, and emission area would be known for all emission sites. However, it is merely impossible to do so except for electrodes engineered to have a specific field enhancement factor.

Tomaschke and Alpert [21] examined the collective field emission from 100 emission sites, each randomly assigned value of beta and emitting area, and the accumulation of all the emitters' contributions make up the total current:

$$I = \sum_{i=1}^N A_i \frac{C_1 E_i^2}{\phi_i t(y)^2} e^{-\frac{C_2 \phi_i^{3/2} v(y)}{E_i}} \quad (3)$$

Their findings revealed that the total emission was closely aligned with a linear Fowler-Nordheim plot (assuming that $t(y)$ and $v(y)$ are unity). Therefore, they could find an effective field enhancement factor and a total field-emitting area. Several studies [22, 23] have tried to find an effective field enhancement factor for broad-area cathodes. The common observation of these studies is that as the applied electric field increases, β_{eff} decreases. As the electric field increases, the lower β_{eff} areas on the surface begin to contribute more to the current density.

The inability of these models to adapt to more complex geometries and to provide a systematic approach to predict the field emission current from practical electrode geometries was a motivation for the authors to develop a new approach based on an experimental database.

3. Predictive Modeling of Field Emission Current Using Data-Driven Approaches

According to the theoretical overview of field emission, the key parameters of field emission are

classified into these categories: (a) electrostatic parameters that describe the macroscopic field gradient at the cathode surface, (b) geometrical parameters that influence the microscopic field gradient at the cathode surface and the emitting area, and (c) the chemical composition of the cathode surface. This study assumes that the vacuum level and the residual gas composition remain reasonably constant across different tests.

In this study, the data collected are processed and utilized to train a machine learning model to predict the field emission current of the cathode based on a given voltage. The objective is to transition from using a curve-fitting Fowler-Nordheim equation to a generalized, nonlinear model that more accurately captures the relationship between cathode voltage and current, incorporating the described statistical features. This is depicted in Figure 2.

At the center of this process is machine learning (ML) model training, which integrates input from three primary groups: experimental measurements, electric field simulation, and optical microscopy. Additionally, factors such as work function and cathode area are considered, ensuring a holistic approach to model training.

Starting with Experimental Measurements, the process begins with measuring the current-voltage ($I - V$) characteristics. This involves calculating the voltage drop across the series resistor and subsequently adjusting the measured voltage and current to obtain the actual cathode voltage, $V_{cathode}$ and current, $I_{cathode}$. $V_{cathode}$ is used as one of the input parameters and $I_{cathode}$ is the target quantity for the approximation.

In parallel, Electric Field Simulation involves simulating the geometry explained in Section 4, filtering fields above 5 MV/m to focus on significant emission areas, applying a Gaussian mixture model (GMM) for statistical analysis, and extracting relevant features that make up the input matrix.

Optical microscopy is used to collect detailed surface information. This involves obtaining depth profiles, determining probability distributions, fitting skewed Gaussian models, and extracting roughness features. These microscopic characteristics provide a granular view of the emission surface, adding depth to the feature set used in the ML model training.

Finally, factors such as work function, which affects electron emission properties, and cathode area, which influences emission intensity, are incorporated. Together, these diverse inputs ensure

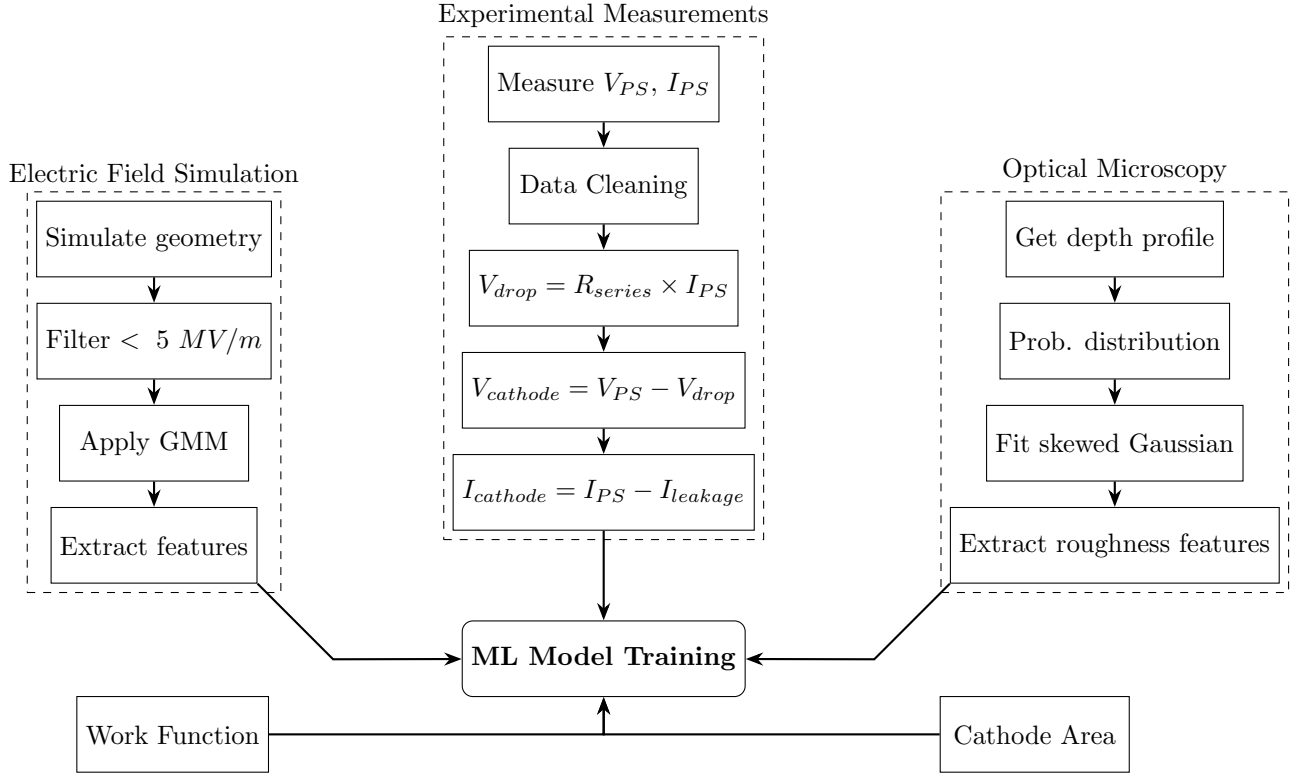


Figure 2: Flowchart illustrating the feature extraction and machine learning model training process for field emission.

that the ML model is trained on a robust dataset, which includes empirical measurements, theoretical simulations, and microscopic surface characteristics, allowing accurate and reliable predictions of field emission behavior.

4. Experiment Setup

Figure 3 shows the experiment setup for field emission testing on different cathode materials. The electrode assembly involves a negatively charged cathode, a dielectric spacer (made from MACOR), and a grounded anode (fabricated from stainless steel). The assembly is housed within a vacuum chamber, where a roughing pump and a turbo pump maintain a pressure below 1×10^{-8} Torr. The high voltage is transmitted from the power supply to the cathode using a cable along with a resistor limiting current $1 M\Omega$. The power supply voltage and current were recorded at a rate of one sample per second. The voltage is increased incrementally to follow a current conditioning method from $0 kV$ to $80 kV$. During the experiment, measurements of the anode current, vac-

uum pressure, and X-ray intensity were taken along with the voltage and current read at the power supply terminal. Observations of discharges were made visually through a chamber window using a high-speed camera equipped with wide-field optics to detect any discharge inside the vacuum chamber.

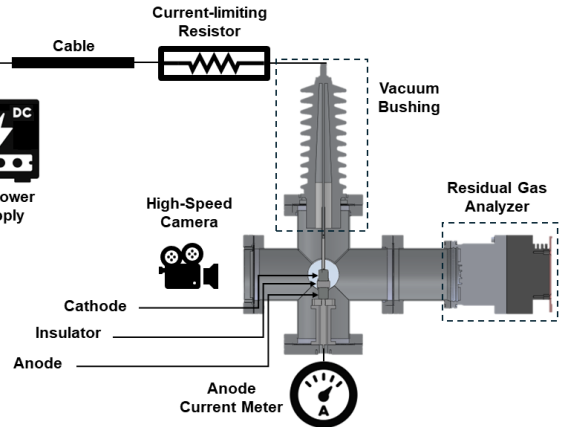
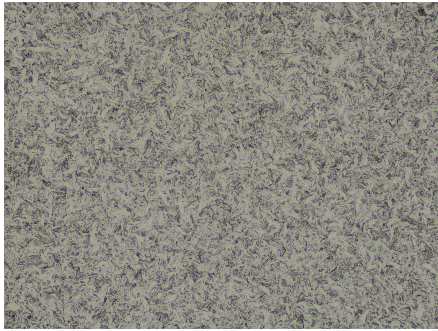


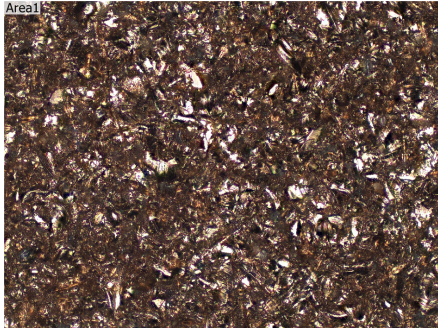
Figure 3: Schematic representation of the apparatus for the measurement of field emission current.

4.1. Sample Preparation

All specimens for testing are made from bulk materials. The selection of cathode materials involved molybdenum (type 361) with a purity of 99.95%, titanium (grade 2), and copper (grade 101). The specimens were shaped using computer numerical control (CNC) machining and then finished by turning and manual sanding to achieve a surface roughness of $2\ \mu\text{m}$ or finer. Certain specimens were intentionally grit-blasted to increase surface roughness. Figure 4 illustrates one copper and one molybdenum specimen under 10x optical microscopy.



(a) Polished molybdenum.



(b) Grit blasted copper.

Figure 4: The surface morphology of two specimens magnified at 10x under the 3D surface profiler laser microscope.

Following fabrication, the samples were subjected to a cleaning protocol to remove hydrocarbons and other residues that remain from the manufacturing process as much as possible. Initially, the sample was washed with hot soapy water in a sink to remove the primary contaminants. Subsequently, it was subjected to a 15-minute ultrasonic cleaning cycle with hot soapy water. After being rinsed, the sample was transferred to another ultrasonic cleaner containing deionized water for a brief two-minute cleansing. Subsequently, the sample is im-

mersed in an ultrasonic cleaner filled with isopropyl alcohol (IPA) for an additional 15 minutes. The final step includes drying the sample with a lint-free cloth in a class-10,000 cleanroom.

5. Data Preprocessing

To prepare the raw experimental and simulation data for use in a data-driven model, the data must be cleaned and enriched with other known information. The flow chart in Figure 2 shows the steps that we will discuss in the rest of the section.

5.1. Experimental Data

As mentioned above, more than 259 hours of data have been used in this study. The processing of the data was done with the aim that only conditioned current values for each voltage level are acquired.

In the next step, the tests are automatically separated by following the rise and fall in voltage trend in the dataset.

The first step is the removal of the data points where, due to electromagnetic interference and transient faults, the voltage or current has not been properly stored. In the next step, the tests are automatically separated by following the rise and fall of the cathode voltage in the dataset. Any test without complete information on the cathode condition is deleted. Data points where the voltage setpoint and the voltage measurement are not within 10% are also removed.

During each test, the settled voltages are detected, i.e., the voltage points where the cathode has been conditioned. In the case of current, current spikes due to discharges are omitted from the dataset and only stable-field emission current values are used.

The experimental data used in this model are measurements of cathode voltage, $V_{cathode}$, and cathode current, $I_{cathode}$. However, in the experimental setup, we measure the current of the power supply, I_{PS} , and the voltage, V_{PS} . Since there is a series resistor, R_{series} , in line between the power supply and the vacuum chamber, the measured voltage (V_{PS}) includes an additional voltage due to the drop across the resistor. Therefore, the cathode voltage should be calculated as $V_{cathode} = V_{PS} - R_{series} \times I_{PS}$.

Additionally, the current, I_{PS} , captures not only the cathode current but also any leakage current, $I_{leakage}$, such as that of the corona in the exposed

electrodes. Therefore, the baseline leakage current as a function of the power supply voltage from the actual cathode measurement at each corresponding voltage level. By deducting the leakage current from the measured current, we acquire the cathode current $I_{cathode} = I_{PS} - I_{leakage}$. Ultimately, we obtain a matrix containing numerous pairs of $V_{cathode}$ and $I_{cathode}$, with each pair representing the total field emission current of a specific cathode under a particular voltage.

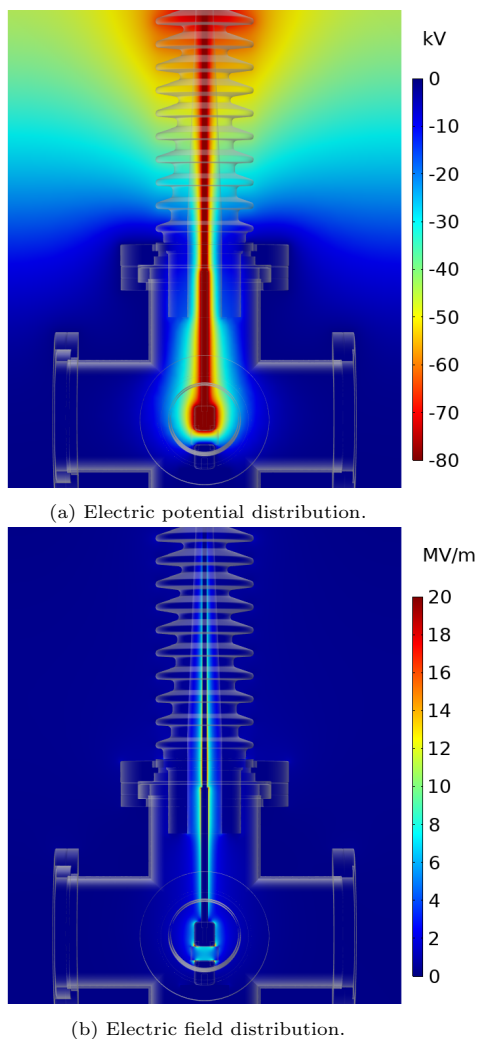


Figure 5: The electrostatic simulation of the high voltage assembly with cathode at -80kV.

5.2. Electrostatic Simulation

The field emission of electrons is strongly related to the strength of the electric field on the cathode surface, as discussed in Section 2. For a single emitter, the field at that emission site is

needed to calculate the emission current based on the Fowler-Nordheim expression. However, in the case of broad-area emission, the electron current stems from a multitude of emission sites. The net electric field at each of these emission sites is dependent on (1) the macroscopic electric field and (2) the microscopic field enhancement factor. In this study, the objective is to incorporate these parameters statistically. As a first step, the macroscopic electric field at the surface of the cathode is simulated electrostatically.

Figure 5 shows the distribution of the electric field in the periphery of the cathode. To feed the machine learning model, this study uses statistical features that describe the inhomogeneity of the electric field distribution. For a virgin electrode, there is a threshold field in the range of 5 – 15 MV/m associated with the initial switch-on of the field emission current [24]. Therefore, the electric field values below 5 MV/m are included in the probability distribution of electric field.

A Gaussian mixture model (GMM) is used to represent an inhomogeneous electric field distribution at the surface of a cathode by assuming that the field distribution is composed of multiple Gaussian components, each representing a distinct region with its own mean and variance. This model allows for the accommodation of complex and multi-modal field distributions, which are common in practical scenarios due to irregularities in material properties and geometric configurations. Each component in the GMM can be thought of as a local 'peak' or 'valley' in the field intensity, and the overall model provides a probabilistic framework for estimating the likelihood of field strengths at different points on the cathode surface. The sensitivity analysis of model prediction with respect to the number of components are discussed in section 7.

Figure 6 demonstrates the distribution of the electric field intensity using four Gaussian distributions. Therefore, eight statistical features are used to explain the contribution of the electric field to the field emission in the model. After benchmarking different numerical models. A sensitivity analysis of the number of components in the GMM approximation is performed to find the optimal mixture model.

5.3. Optical Microscopy

For broad-area electrodes, it is well-established that field enhancement can exhibit significant spatial variability. Consequently, an effective ap-

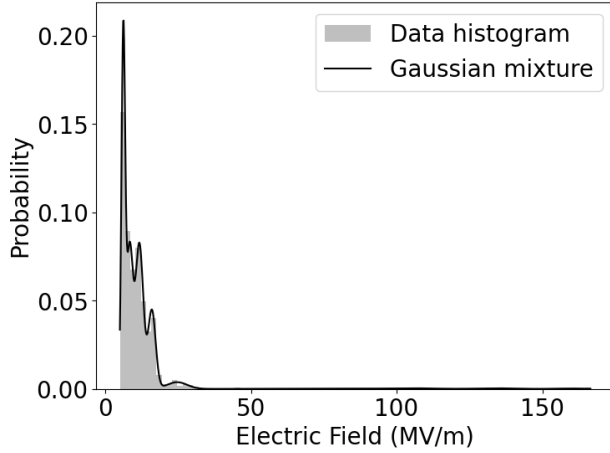


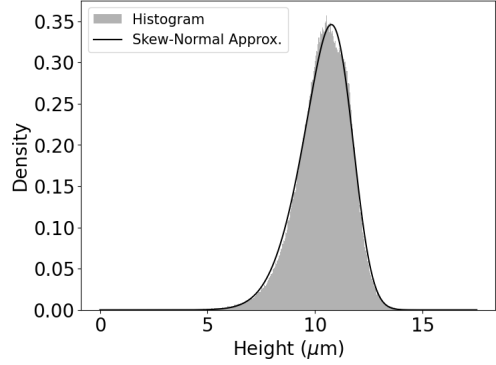
Figure 6: Probability distribution of electric field at the surface of cathode.

proximation of surface microprotrusions is essential to capture the extensive variance in the current-voltage measurements. In this study, we employ laser microscopy to characterize the surface profile of the sample, thereby enabling a detailed examination of the microscopic features of the cathode surface. The chemical composition has previously been analyzed by the authors in [25] and is not repeated here for brevity.

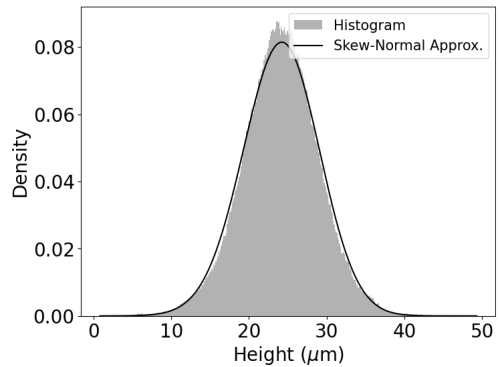
Surface roughness was determined with a Keyence VK X3050 3D surface profiler. Each specimen is examined using the laser microscope and the height array for an area of $1 \mu\text{m} \times 1 \mu\text{m}$ at the center of the cathode surface. Due to the uniform surface preparation process, the $1 \mu\text{m}^2$ area can provide a valid representation of the total cathode area. Figure 7 depicts the probability distributions of the surfaces of two specimens shown in Figure 4. If we plot the histogram of the height distribution, a skewed Gaussian distribution can approximate the projection heights of the probability distribution. Therefore, three statistical features incorporate a microscopical fingerprint.

6. Numerical Results

After the data have been processed and the datasets have been created, a collection of physical and environmental parameters is used as input features, and the cathode current vector serves as the target vector. The layout of a single row of input/output features can be seen in Figure 8.



(a) Polished molybdenum.



(b) Grit blasted copper.

Figure 7: The probability distribution of projection heights for two specimens.

Only stable field emission current data points post-conditioning are utilized in the modeling. The total count of data points is 920, which will be divided into 80% for training and 20% for testing. The problem at hand is identified as a regression analysis. This section benchmarks several well-known models. Given the widespread use of these models in different areas of machine learning, descriptions of each algorithm are avoided (for comprehensive information on these models, refer to [26]).

The hyperparameters of each model can be adjusted to improve the accuracy of the prediction. We begin with simple models such as linear regression, and then move toward more advanced models. Performance metrics used include mean squared error (MSE), mean absolute error (MAE), and coefficient of determination (R^2 score). To find the optimal hyperparameters, we utilize the Bayesian optimization method, specifically the tree-structured Parzen estimator, with the aim of maximizing the

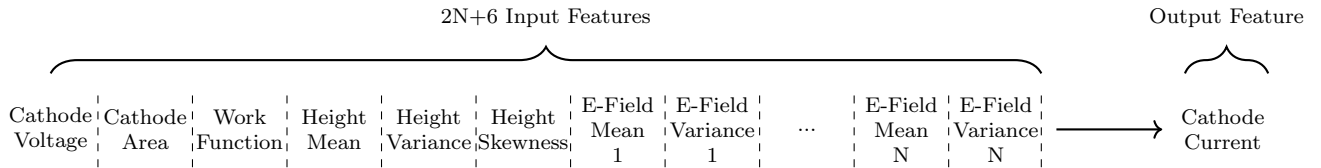


Figure 8: The structure of single datapoint in the input and output arrays.

R^2 score. The models are developed in Python using open-source libraries, including `Pandas`, `NumPy`, `TensorFlow`, `Scikit-learn`, `Optuna`, and `XGBoost`.

6.1. Linear Regression

Linear regression is the simplest regression model if a linear correlation is anticipated between the input and the target variable. In the first attempt, we have employed Ridge and Lasso in linear regression as regularization strategies to attenuate overfitting.

The focus of hyperparameter tuning is on the regularization parameter α , exploring a logarithmic scale from 10^{-4} to 10^4 . Through 1000 trials, the optimal α values for Ridge and Lasso were found to be approximately 26.58 and 1.07, respectively. With these optimal parameters, the models were trained on the training dataset and then evaluated on the test dataset. The Ridge model achieves an MSE of 1414.1, an MAE of 26.9, and an R^2 score of 43.8%. In contrast, the Lasso model achieves an MSE of 1529.8, an MAE of 27.4, and an R^2 score of 39.2%. The R^2 score indicates that the Ridge regression model explains approximately 43.8% and 39.2% of the variance in the target variable, respectively. The performance of these models indicates a necessity for more sophisticated modeling techniques to better capture the highly nonlinear relationship between field emission current and its input features, thereby enhancing predictive accuracy.

6.2. Support Vector Regression

Support Vector Regression (SVR) has shown to be effective in high-dimensional spaces and when a certain tolerance margin within the model is required. It often achieves good performance with non-linear relationships when the suitable kernel is employed. In our implementation of SVR, hyperparameter optimization was carried out focusing on the regularization parameter, α , which ranged from 10^{-4} to 10^4 , ϵ spanning from 10^{-4} to 10^2 defining the tolerance margin where no penalties are applied for errors, kernel types including linear, polynomial, radial basis function (RBF), and sigmoid. From

more than 1000 trials, the optimal parameters determined were $\alpha = 4967.8$, $\epsilon = 0.27$, RBF kernel, and its tuning parameter $\gamma = 3.06$, which describes the extent of influence of a single training example.

Using these optimal parameters, the SVR model was trained on the full training dataset and evaluated on the test dataset. The SVR model achieved an MSE of 1051.67, an MAE of 18.67, and an R^2 score of 58.2%. The improvement in predictive accuracy, compared to the Ridge and Lasso regression models, highlights the higher efficacy of SVR in capturing nonlinear relationships within this set of data. Nonetheless, the results suggest potential for further enhancements in predictive performance.

6.3. Random Forest Regression

In the next model, we explore random forest regression (RFR), an ensemble learning method that builds multiple decision trees and combines them to achieve more accurate and stable predictions. This approach effectively handles complex interactions and nonlinearities, providing better generalization and feature importance scores, though it is less interpretable and computationally intensive. The key optimization parameters included the number of estimators (from 100 to 10000), maximum tree depth (from 10 to 1000), minimum samples for splitting (from 2 to 20) and leaf nodes (from 1 to 20), maximum number of features for splitting (from 4 to 14) and bootstrap sampling. Through 1000 optimization trials, the optimal parameters identified were 7965 estimators, a maximum depth of 316, a minimum of 2 samples for node splitting, 2 samples per leaf node, the maximum number of features of 14 without bootstrapping.

The RFR model achieved an MSE of 82.6, an MAE of 4.4, and an R^2 score of 96.7%. This high R^2 score indicates that the random forest model accounts for approximately 97% of the variance in the target variable, demonstrating its superior performance in terms of capturing complex relationships within the dataset compared to previous models.

6.4. Gradient Boosting Regression

Further extending our analysis, we applied gradient boost regression (GBR), another ensemble technique that builds models sequentially to focus on the errors of previous models, often enhancing accuracy. GBRs are effective in achieving high predictive accuracy, but can be prone to overfitting, sensitive to noisy data and outliers, and require meticulous parameter tuning. The optimization process involved parameters such as the number of estimators (100 to 10,000), learning rate (0.01 to 0.5), maximum depth (1 to 10), minimum samples to split a node (2 to 20), minimum samples in a leaf node (1 to 20), subsample ratio (0.25 to 1.0), and the maximum features to split. After 1000 trials, the optimal parameters identified were 7895 estimators, a learning rate of 0.43, a maximum depth of 2, 2 samples to split a node, 10 samples per leaf node, a subsample ratio of 0.985, and the maximum number of features of 13.

The GBR model achieved an MSE of 42.1, an MAE of 3.2, and an R^2 score of 98.2%. This high R^2 score indicates that the gradient boost model accounts for more than 98% of the variance in the target variable. The significant reduction in error metrics and the impressive R^2 score underscore the robustness of gradient boosting to capture complex data patterns and relationships.

6.5. Extreme Gradient Boosting Regression

We explored the performance of the extreme gradient boosting regression (XGBR). Compared to GBR, XGBR uses more advanced regularization techniques, handles missing values more efficiently, provides parallel and distributed computing, and offers more options for customization. The parameters considered included the column subsampling ratio (varying from 0.1 to 1.0), which determines the proportion of features used for each tree, the learning rate (from 0.01 to 0.3), the maximum depth of the trees (from 3 to 50), the L1 regularization term on weights, α (varying from 0.1 to 100), the L2 regularization term on weights, λ (from 10^{-8} to 1), and the number of boosting rounds (from 100 to 1000). Additional parameters include minimum loss reduction required for the partition of leaf nodes, γ (from 10^{-8} to 1), the minimum weight required to create a new tree node (from 1 to 10), and the controlling factor for the balance of positive and negative weights (between 0.1 and 10).

The best tuning results for the XGBR model indicate that the optimal parameters include a tree feature selection rate of approximately 36%, a learning rate of about 29.4%, and a maximum tree depth of 29. Regularization was achieved with an α value of approximately 0.15 and a λ value near 0.002, while the model was trained using 604 estimators. The optimal model also featured a γ value of around 0.003, a sample rate of approximately 64%, and a minimum child weight of 1. Additionally, the scale for positive class weights was set at about 7.56. The best model achieved an R^2 score of 90.9%, an MSE of 229.0 and an MAE of 7.5. The results demonstrate a relatively robust performance of the optimal XGBR model, but inferior to GBR and RF, due to the ineffectiveness of the extra regularization parameters given the size of the dataset and the number of features.

6.6. Neural Network Regression

Neural networks are highly flexible and powerful, capable of learning very complex patterns and relationships in large and complex datasets. They offer significant flexibility, but require careful tuning, are prone to overfitting, and generally lack interpretability. More data and computational resources might be needed.

The neural network architecture was optimized by fine-tuning several crucial parameters. These included the number of hidden layers (varying from 1 to 8) and the number of units per layer (ranging from 16 to 128), the activation function (chosen from linear, ramp, softmax, sigmoid, hyperbolic tangent, exponential and scaled exponential linear units.), the dropout rate (fluctuated between 0.0 and 0.5), the learning rate (η) from $1e^{-5}$ to $1e^{-1}$, and the optimizer including various versions of adaptive moment estimation (Adam, Adamax, NAdam), root mean square propagation (RMSProp) and gradient-based optimization methods (SGD, AdaDelta, AdaGrad, FTRL). In addition, the number of epochs was up to 200 with early stopping on patience with 5 epochs, and the batch size was adjusted between 32 and 64.

The optimal hyperparameters identified were as follows: a network architecture consisting of 2 layers (first with 32 neurons and 12% dropout, and second with 128 neurons and 31% dropout), ramp activation function, RMSProp optimizer, a 2.4% learning rate and a batch size of 32. The best result from the neural network model achieved an MSE,

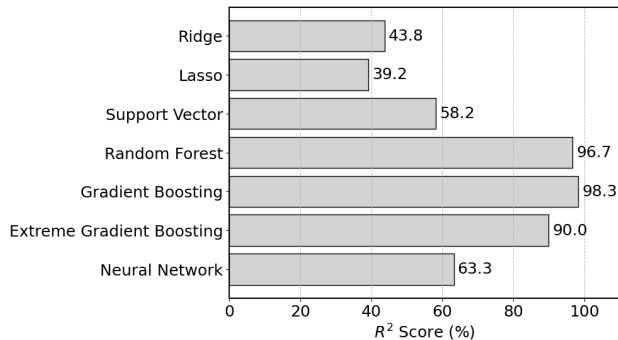


Figure 9: Performance comparison among various machine learning models.

MAE and R^2 values of 922.9, 20.3 and 63.4%, respectively. While this performance surpasses that of linear models, it does not match the effectiveness of ensemble methods. The low number of layers in the optimal shows the need of a larger dataset and possibly a higher number of features to optimize their performance.

7. Discussion

The performance of various regression models on the given dataset, indicated by their R^2 scores, is summarized in Figure 9. The results reveal that traditional linear models such as Ridge and Lasso exhibit relatively low R^2 scores of 43.8% and 39.2%, respectively, suggesting a limited ability to capture complex relationships in the data. In contrast, Support Vector Regression achieves a higher score of 58.2%, indicating its ability to handle nonlinear patterns slightly better than Ridge and Lasso. However, it is the ensemble methods that significantly outperform the others: random forest, gradient boosting, and extreme gradient boosting show R^2 scores of 96.7%, 98.3%, and 90.0%, respectively. These high scores highlight the strength of ensemble learning in reducing variance and bias through the aggregation of multiple models. In particular, the performance of the neural network was not as good as that of the ensemble models, with a R^2 score of 63.3%.

The superior performance of ensemble methods like random forest and gradient boosting can be attributed to their inherent ability to combine the strengths of multiple decision trees, thereby enhancing the overall robustness and accuracy of the model. Random forest achieves high performance

through bagging, which reduces overfitting by averaging multiple decision trees trained on different subsets of the data. Gradient boosting, on the other hand, builds trees sequentially, each correcting the errors of its predecessor, leading to a highly accurate model, as evidenced by its highest R^2 score of 98.3. Extreme gradient boosting, a more efficient and regularized version of gradient boosting, also performs exceptionally well with a score of 90.0, balancing computational efficiency and accuracy. Neural networks, with their deep learning capabilities, perform better than traditional linear models but fall short of ensemble methods, likely due to their need for extensive tuning and larger datasets to achieve peak performance. The variation in these scores underscores the importance of model selection based on the specific characteristics and complexity of the dataset at hand.

A sensitivity analysis on the effect of the GMM components (1 to 9) on the electric field approximation was performed to further enhance the accuracy of the GBR prediction. The R^2 score remained between 97.0% and 98.6% without any trend, indicating minimal impact from varying electric field approximation complexity. This was expected because of the identical cathode geometry in all data points. The impact is expected to be more significant with the varied cathode geometries.

8. Conclusion

In pursuit of a robust yet practical model to predict total field emission from broad-area electrodes, this study approached the problem with an emphasis on extensive experimental data. We paired the experimental data with the electrostatic field distribution, surface profile, and material information to build a matrix of input features for prediction. Upon benchmarking various machine learning models, we found that the ensemble models, especially the gradient boosting regression, perform remarkably well, achieving over 98% accuracy. Neural neural networks of different depths did not offer improved results.

The findings presented herein should not be considered definitive. As the number of features and/or the size of the dataset expands, more sophisticated models may become necessary. These advanced models will potentially encapsulate a broader range of variability and, it is anticipated, will eventually evolve into a sufficiently robust framework capable of accurately predicting the field emission current

from an electrode. One should also note that more statistical features may hinder the practicality and cost of using such models.

Future studies will focus on larger datasets that encompass multiple geometries while incorporating a more detailed chemical composition of the cathode surface.

Acknowledgment

We express our gratitude to Alexander Fiore, Dr. Craig Miller and Professor Rod Latham for their insightful discussions and thorough review of our manuscript.

Data Availability

The data that support the findings of this study are available from the corresponding authors upon reasonable request.

References

- [1] J. E. Lilienfeld, Einiges Experimentelle zur autoelektronischen Entladung, *Zeitschrift für Physik* 15 (1) (1923) 46–50. doi:10.1007/BF01330454. URL <https://doi.org/10.1007/BF01330454>
- [2] W. D. Coolidge, Use of very high-voltage in vacuum tubes, *Journal of the A.I.E.E.* 47 (3) (1928) 212–213. doi:10.1109/JAIEE.1928.6538023.
- [3] W. Schottky, Über kalte und warme Elektronenentladungen, *Zeitschrift für Physik* 14 (1) (1923) 63–106. doi:10.1007/BF01340034. URL <https://doi.org/10.1007/BF01340034>
- [4] R. A. Millikan, C. F. Eyring, Laws governing the pulling of electrons out of metals by intense electrical fields, *Phys. Rev.* 27 (1926) 51–67. doi:10.1103/PhysRev.27.51. URL <https://link.aps.org/doi/10.1103/PhysRev.27.51>
- [5] R. A. Millikan, C. C. Lauritsen, Relations of field-currents to thermionic-currents, *Proceedings of the National Academy of Sciences* 14 (1) (1928) 45–49. doi:10.1073/pnas.14.1.45. URL <https://www.pnas.org/doi/abs/10.1073/pnas.14.1.45>
- [6] O. W. Richardson, On the extraction of electrons from cold conductors in intense electric fields, *Proceedings of the Royal Society of London. Series A, Containing Papers of a Mathematical and Physical Character* 117 (778) (1928) 719–730. doi:10.1098/rspa.1928.0031. URL <https://royalsocietypublishing.org/doi/abs/10.1098/rspa.1928.0031>
- [7] J. R. Oppenheimer, Three notes on the quantum theory of aperiodic effects, *Phys. Rev.* 31 (1928) 66–81. doi:10.1103/PhysRev.31.66. URL <https://link.aps.org/doi/10.1103/PhysRev.31.66>
- [8] R. H. Fowler, L. Nordheim, Electron emission in intense electric fields, *Proceedings of the Royal Society of London. Series A, Containing Papers of a Mathematical and Physical Character* 119 (781) (1928) 173–181. doi:10.1098/rspa.1928.0091. URL <https://royalsocietypublishing.org/doi/abs/10.1098/rspa.1928.0091>
- [9] E. Z. Engelberg, Y. Ashkenazy, M. Assaf, Stochastic model of breakdown nucleation under intense electric fields, *Physical review letters* 120 (12) (2018) 124801.
- [10] V. Jansson, E. Baibuz, A. Kyrtsakis, S. Vigonski, V. Zadin, S. Parviainen, A. Aabloo, F. Djurabekova, Growth mechanism for nanotips in high electric fields, *Nanotechnology* 31 (35) (2020) 355301. doi:10.1088/1361-6528/ab9327. URL <https://dx.doi.org/10.1088/1361-6528/ab9327>
- [11] J. D. Zuber, K. L. Jensen, T. E. Sullivan, An analytical solution for microtip field emission current and effective emission area, *Journal of Applied Physics* 91 (11) (2002) 9379–9384. doi:10.1063/1.1474596. URL <https://doi.org/10.1063/1.1474596>
- [12] C. J. Edgcombe, Development of fowler-nordheim theory for a spherical field emitter, *Phys. Rev. B* 72 (2005) 045420. doi:10.1103/PhysRevB.72.045420. URL <https://link.aps.org/doi/10.1103/PhysRevB.72.045420>
- [13] C. J. Edgcombe, N. de Jonge, Deduction of work function of carbon nanotube field emitter by use of curved-surface theory, *Journal of Physics D: Applied Physics* 40 (14) (2007) 4123. doi:10.1088/0022-3727/40/14/005. URL <https://dx.doi.org/10.1088/0022-3727/40/14/005>
- [14] A. Kyrtsakis, J. P. Xanthakis, Derivation of a generalized fowler–nordheim equation for nanoscopic field-emitters, *Proceedings of the Royal Society A: Mathematical, Physical and Engineering Sciences* 471 (2174) (2015) 20140811. doi:10.1098/rspa.2014.0811. URL <https://royalsocietypublishing.org/doi/abs/10.1098/rspa.2014.0811>
- [15] B. M. Cox, The nature of field emission sites, *Journal of Physics D: Applied Physics* 8 (17) (1975) 2065. doi:10.1088/0022-3727/8/17/008. URL <https://dx.doi.org/10.1088/0022-3727/8/17/008>
- [16] C. Athwal, R. Latham, The effect of the applied field on the energy spectra of electrons field emitted from microscopic sites on broad-area copper electrodes, *Physica B+C* 104 (1) (1981) 189–195. doi:https://doi.org/10.1016/0378-4363(81)90050-4. URL <https://www.sciencedirect.com/science/article/pii/0378436381900504>
- [17] C. S. Athwal, R. V. Latham, Switching and other non-linear phenomena associated with prebreakdown electron emission currents, *Journal of Physics D: Applied Physics* 17 (5) (1984) 1029. doi:10.1088/0022-3727/17/5/017. URL <https://dx.doi.org/10.1088/0022-3727/17/5/017>
- [18] R. E. Hurley, Electrical phenomena at the surface of electrically stressed metal cathodes. i. electroluminescence and breakdown phenomena with medium gap spacings (2–8 mm), *Journal of Physics D: Applied Physics* 12 (12) (1979) 2229. doi:10.1088/0022-3727/12/12/026.

- URL <https://dx.doi.org/10.1088/0022-3727/12/12/026>
- [19] H. M. Miller, Obtaining numerical values for the elliptic emission functions used in calculating electron emission from surfaces, *Journal of Vacuum Science and Technology* 17 (3) (1980) 691–695. doi:10.1116/1.570543. URL <https://doi.org/10.1116/1.570543>
- [20] D. A. Kirkpatrick, A. Mankofsky, K. T. Tsang, Analysis of field emission from three-dimensional structures, *Applied Physics Letters* 60 (17) (1992) 2065–2067. doi:10.1063/1.107090. URL <https://doi.org/10.1063/1.107090>
- [21] H. Tomaschke, D. Alpert, Field Emission from a Multiplicity of Emitters on a Broad-Area Cathode, *Journal of Applied Physics* 38 (2) (1967) 881–883. doi:10.1063/1.1709430. URL <https://doi.org/10.1063/1.1709430>
- [22] Y. Feng, J. P. Verboncoeur, A model for effective field enhancement for Fowler–Nordheim field emission, *Physics of Plasmas* 12 (10) (2005) 103301. doi:10.1063/1.2103567. URL <https://doi.org/10.1063/1.2103567>
- [23] G. A. Farrall, Numerical Analysis of Field Emission and Thermally Enhanced Emission from Broad-Area Electrodes in Vacuum, *Journal of Applied Physics* 41 (2) (1970) 563–571. doi:10.1063/1.1658714. URL <https://doi.org/10.1063/1.1658714>
- [24] R. Latham, N. Xu, ‘electron pin-holes’: the limiting defect for insulating high voltages by vacuum, a basis for new cold cathode electron sources, *Vacuum* 42 (18) (1991) 1173–1181. doi:[https://doi.org/10.1016/0042-207X\(91\)90127-5](https://doi.org/10.1016/0042-207X(91)90127-5). URL <https://www.sciencedirect.com/science/article/pii/0042207X91901275>
- [25] M. Borghei, D. Velazquez, R. McMullen, G. Latchford, B. Riordan, R. Langtry, Impact of direct current conditioning on cathode dark current in high vacuum, in: 2023 30th International Symposium on Discharges and Electrical Insulation in Vacuum (ISDEIV), 2023, pp. 74–77. doi:10.23919/ISDEIV55268.2023.10199791.
- [26] C. M. Bishop, N. M. Nasrabadi, *Pattern recognition and machine learning*, Vol. 4, Springer, 2006.